Proceedings of ASME Turbo Expo 2014: Turbine Technical Conference and Exposition
GT2014
June 16 – 20, 2014, Düsseldorf, Germany

GT2014-25399

A TEST RIG FOR THE INVESTIGATION OF THE PERFORMANCE AND FLOW FIELD OF TESLA FRICTION TURBINES

Constantin Schosser*
Technische Thermodynamik, MB 5.1
Universität der Bundeswehr München
D-85577 Neubiberg, Germany
Email: constantin.schosser@unibw.de

Stefan Lecheler
Technische Thermodynamik, MB 5.1
Universität der Bundeswehr München
D-85577 Neubiberg, Germany
Email: stefan.lecheler@unibw.de

Michael Pfitzner
Institut für Thermodynamik, LRT 10
Universität der Bundeswehr München
D-85577 Neubiberg, Germany
Email: michael.pfitzner@unibw.de

ABSTRACT

The paper summarizes the development and optimization of a flexible test facility for 3D tomographic PIV/PTV measurements of the flow field in the rotor gap of a Tesla friction turbine and performance evaluations. The main aim of the experiment will be the validation of CFD simulations. Another intention is to gain a deeper understanding of the flow phenomena in the gap. The extension of existing theoretical investigations lead to an improved knowledge of dimensioning such bladeless turbines with the goal of maximum power and efficiency. The mechanical design of the rotor, based on these equations, was optimized for a minimal deformation and low mechanical stress. Modal and harmonic response analyses due to imbalance forces have been performed to ensure low vibrations during operation. The design of the feed and guide vanes have been optimized for uniformity of the flow entering the Tesla disk's gap. The rotor outlet is optimized to achieve minimal pressure loss at the intended exit swirl angle. For the demonstration of the measurement technique preliminary tomographic PIV/PTV tests have been carried out. The measurement, safety monitoring and feedback-control software was developed for running on a National Instruments compact RIO real-time target.

Keywords: Tesla friction turbine, CFD optimization, tomographic PIV/PTV, LabVIEW real-time, FPGA

*Corresponding author.

NOMENCLATURE

α	flow angle at rotor inlet or stator outlet	$[^\circ]$
β	dimensionless friction parameter	$[-]$
μ	dynamic viscosity	$[\mathrm{Pa \cdot s}]$
ν	kinematic viscosity	$[\mathrm{m^2/s}]$
ρ	density	$[\mathrm{kg/m^3}]$
τ	shear stress	$[\mathrm{Pa}]$
φ	angle, cylindrical coordinate	$[^\circ]$
ω	angular velocity	$[\mathrm{1/s}]$
Ω	dimensionless angular velocity ratio	$[-]$
c	relative circumferential velocity	$[\mathrm{m/s}]$
d	rotor diameter	$[\mathrm{m}]$
e	gap width blockage error	$[-]$
f	rotational frequency	$[\mathrm{Hz}]$
n	revolution speed	$[\mathrm{rpm}]$
p	pressure	$[\mathrm{Pa}]$
r	cylindrical coordinate, rotor radius	$[\mathrm{m}]$
s	half of the rotor gap width	$[\mathrm{m}]$
u	absolute circumferential velocity	$[\mathrm{m/s}]$
v	radial velocity	$[\mathrm{m/s}]$
w	resultant absolute velocity	$[\mathrm{m/s}]$
z	cylindrical coordinate	$[\mathrm{m}]$
A	area	$[\mathrm{m^2}]$
C_p	dimensionless absolute power coefficient	$[-]$
C_{pt}	dimensionless economical power coefficient	$[-]$
C	dimensionless relative circumferential velocity	$[-]$
P	dimensionless pressure ratio	$[-]$
R	dimensionless rotor radius ratio	$[-]$
Re	Reynolds number	$[-]$
U	dimensionless absolute circumferential velocity	$[-]$

V	dimensionless radial velocity	$[-]$
W	dimensionless absolute resultant velocity	$[-]$
Z	dimensionless gap width	$[-]$

SUBSCRIPTS

$1,2$	rotor inlet, rotor outlet
t	total

INTRODUCTION

The first bladeless friction turbine was designed, built and patented by Nicola Tesla in 1913 [1]. A Tesla turbine's rotor consists of several co-rotating disks mounted on a hollow shaft. The flow, driven by a pressure difference enters the rotor at a shallow angle through guide vanes or nozzles at the outer radius of the disks and flows spirally towards the axis of rotation, where the flow leaves the turbine via a hollow shaft (Fig. 1). The momentum exchange between rotor and fluid creates torque and power. The simple and robust design of Tesla friction turbines might offer an economical alternative to conventional turbo machinery, when individual, easily scalable solutions at low cost are required. Especially renewable, sustainable energy technologies might be the field of application, when low investment and maintenance costs are in focus, as suggested by Romanin [2], Lampart [3] and Khan [4]. In the 60s and 70s of the 20th century several theoretical as well as experimental investigations about the Tesla turbine and pump have been carried out by Breiter et. al. [5], Rice [6], Beans [7] and Nendl [8]. In these experiments mainly performance maps (power, torque, rpm) were generated. Flow measurements were not possible for typical turbine gap dimensions ($\leq$1 mm). Nendl performed velocity profile measurements in an untypically wide gap (7 mm) with a poor resolution in 1976 [9]. Now, optical measurement techniques offer the possibility to have a closer look at the flow phenomena in the gap.
Based on the results of a theoretical analysis, a flexible test facility has been designed in order to apply tomographic PIV measurements in the gap of a friction turbine. A second rotor is planned for performance tests in the future.

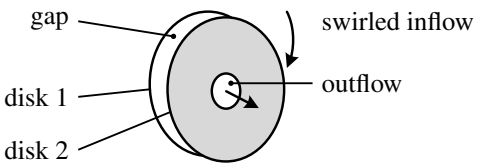

Figure 1. PRINCIPLE OF A TESLA TURBINE

THEORETICAL ANALYSIS

Due to the lack of geometric design criteria of a Tesla turbine, a model for the incompressible, laminar flow through such a rotor has been developed based on the research work of Beans [7]. In contrast to Beans, a fully analytical solution for the pressure has been found, assuming a parabolic velocity profile for the flow between the disks. Wolfram Mathematica has been used for solving the equations. In addition to that, a different definition of the power coefficient leads to an optimization of maximum power for a given pressure difference across the rotor. Furthermore it provides knowledge about the influences of geometrical rotor design on turbine characteristics.

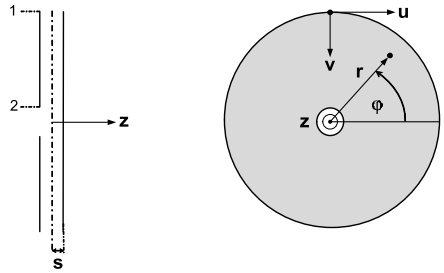

Figure 2. CYLINDRICAL COORDINATESYSTEM

Following Beans and using a semi-infinitesimal control volume

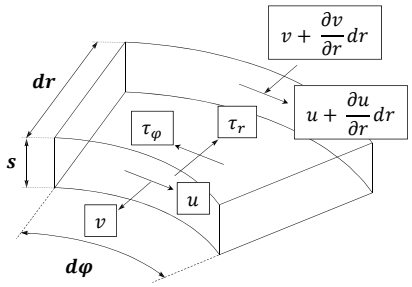

Figure 3. SEMI-INFINITESIMAL CONTROL VOLUME

the steady-state continuity equation [7] yields

$$\frac{d(\rho \cdot r \cdot v)}{dr} = 0, \tag{1}$$

the $\varphi-$ and r-momentum equations [7] are

$$\rho \cdot v \left[\frac{du}{dr} + \frac{u}{r} \right] - \frac{\tau_\varphi}{s} = 0, \tag{2}$$

$$\rho\left[v\frac{dv}{dr}-\frac{u^2}{r}\right]+\frac{dp}{dr}-\frac{\tau_r}{s}=0. \tag{3}$$

The shear stress in r and φ direction, which can be expressed as

$$\tau_\varphi=\mu\left(\frac{dc}{dz}\right),\ \tau_r=\mu\left(\frac{dv}{dz}\right) \tag{4}$$

are computed by assuming parabolic velocity profiles. The absolute velocity is

$$u=c+\omega\cdot r. \tag{5}$$

With the introduction of the dimensionless parameters

$$C=\frac{c}{c_1},\quad U=\frac{u}{u_1},\quad V=\frac{v}{u_1},\quad P=\frac{p}{\rho u_1^2}, \tag{6}$$

Eq. 2 and Eq. 3 can be rewritten in dimensionless variables

$$\frac{dU(R)}{dR}+\left(\frac{1}{R}-2\beta R\right)\cdot U(R)+2\beta\Omega R^2=0, \tag{7}$$

$$\frac{dP}{dR}-V_1^2\cdot\left(\frac{1}{R^3}+\frac{2\beta}{R}\right)-\frac{U(R)^2}{R}=0. \tag{8}$$

Eq. 7 is analytically solved with the boundary condition $U(1)=1$. Eq. 8 is then integrated and subtracted by the integration constant $P(1)$. This leads to the expression for the pressure

$$\begin{aligned}P(R)=\frac{e^{-2\beta}}{2\beta^2}\Big[\frac{1}{R^2}\Big(&2e^{\beta(1+R^2)}\Omega(\beta(\Omega-1)+\Omega)-e^{2\beta R^2}\\&\cdot(\beta(\Omega-1)+\Omega)^2+e^{2\beta}\left(\Omega^2(\beta^2R^4-1)-2\beta^2\Omega R^2\right.\\&\left.+\beta^2(R^2+V_1^2(R^2-1))\right)\Big)+4\beta e^{\beta}\Omega(\beta(\Omega-1)+\Omega)\\&\cdot\left(\mathrm{Ei}(\beta)-\mathrm{Ei}(\beta R^2)\right)-2\beta\left(\beta(\Omega-1)+\Omega\right)^2(\mathrm{Ei}(2\beta)\\&-\mathrm{Ei}(2\beta R^2))+4\beta e^{2\beta}\left(\Omega^2+\beta^2V_1^2\right)\log(R)\Big].\end{aligned} \tag{9}$$

The dimensionless machine parameters used in Eq. 7, 8, 9 are

$$\beta=\frac{3}{2}\cdot\underbrace{\left(\frac{r_1}{s}\right)^2}_{geometry}\cdot\underbrace{\frac{\nu}{v_1r_1}}_{\frac{1}{Re}},\quad\Omega=\frac{r_1\omega}{u_1},\quad R=\frac{r}{r_1}. \tag{10}$$

The friction parameter β is a geometrical factor divided by the Reynolds number, which is mainly dependent on the gap width 2s. With low $\beta-$values the gap width is high, thus low power is generated. The normalized angular disk velocity Ω becomes 1, if the tangential component of the velocity at the inflow equals the disk speed. R is a normalized radius. V_1 is the ratio of radial and tangential inflow velocity components and defines the flow angle at the inlet to the disk gap. With the mass flow $\dot{m}$

$$\dot{m}=A_1\cdot v_1\cdot\rho=2\pi r_1(2s)\cdot v_1\cdot\rho, \tag{11}$$

the absolute power $M\cdot\omega$ for one gap at the outlet radius R_2

$$M\cdot\omega=\int_0^{2\pi}\int_{r_1}^{r_2}\tau_\varphi\cdot r^2\,dr\,d\varphi\cdot\omega=\dot{m}(u_1r_1-u_2r_2)\cdot\omega \tag{12}$$

and $U(R)$ solved from Eq. 7, one possible definition of a dimensionless power coefficient is the absolute power coefficient

$$C_p(R_2)=\frac{M\cdot\omega}{A_1\cdot\rho\cdot u_1^3}=V_1\cdot\Omega\cdot(1-U(R_2)\cdot R_2). \tag{13}$$

A more suitable definition for that is the dimensionless economical power coefficient

$$C_{pt}(R_2)=\frac{M\cdot\omega\cdot\sqrt{\rho}}{A_1\cdot(p_{1,t}-p_2)^{\frac{3}{2}}}=\frac{\rho\cdot u_1^3\cdot C_p(R_2)\cdot\sqrt{\rho}}{\left(p_1+\frac{1}{2}\rho u_1^2-p_2\right)^{\frac{3}{2}}}. \tag{14}$$

It relates power output to the pressure difference across the rotor, computed from Eq. 8. This leads to a radius ratio R for maximum power using a minimal pressure drop across the rotor. Applying rotor radius r_1 and fluid properties, the plots of $C_{pt}(R_2)$ show maximum performance at a relatively high radius ratio R_2 (Fig. 4, 5, 6). Favorable are many disks with small gaps.

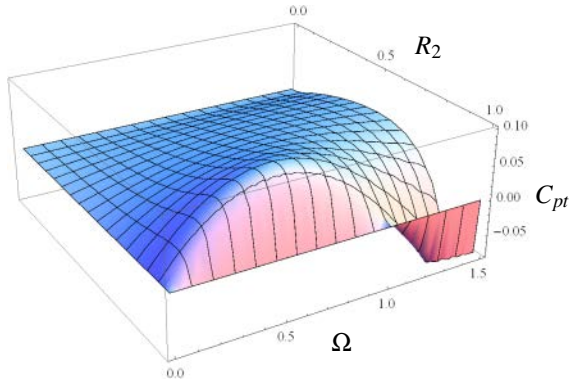

Figure 4. MAPPING OF POWER $C_{pt}(R_2)$ FOR $V_1=0.3,\beta=10$

Here, the optimum angular velocity ratio Ω is 0.65 for $\beta > 10$ (Fig. 4). Absolute maximum power is found at $V_1 \approx 0.3$ for a wide range of β and Ω. This value is slightly dependent on values of Ω (for $\Omega \to 0$, $V_1 \to 0.4$). Fig. 5 exemplarily indicates that maximum performance is found here at $V_1 = 0.3$. The most

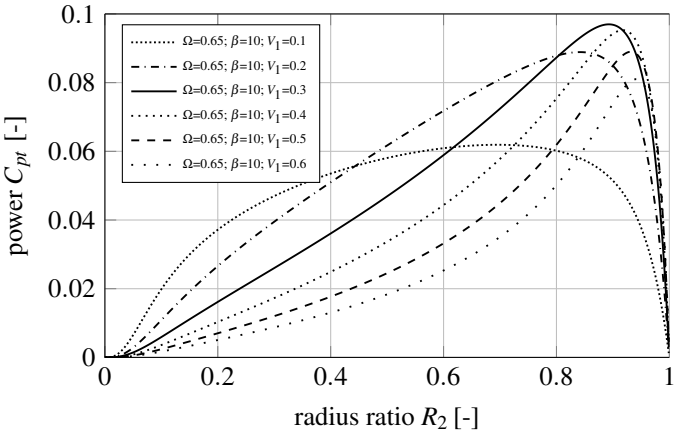

Figure 5. RANGE OF POWER C_{pt} FOR Ω=0.65, β=10

significant dependency of the power output for future technical applications is the parameter β. With $\beta \geq 10$, $U(R)$ the solution of Eq. 7 is generally independent of β. Referring to Fig. 6, maximum power is also generated for $\beta \geq 10$ for the desired turbine geometry and fluid properties. Even if high power is gained with high $\beta-$values, there is an economical optimum for a Tesla turbine dependent on the desired number of gaps. High β values and low gap widths lead to low mass flows and therefore low power for a given number of gaps. Concerning manufacturing, there are limits for a minimum gap width, thus a maximum $\beta-$value.

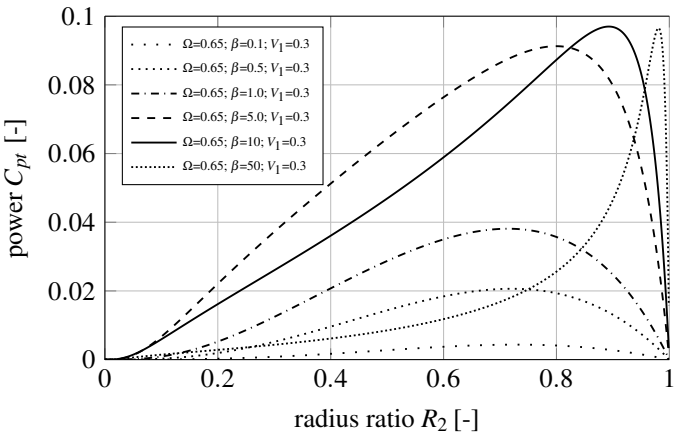

Figure 6. RANGE OF POWER C_{pt} FOR Ω=0.65, V_1=0.3

Beans [7] claimed due to the comparison with his experimental data, that his theoretical investigations present an inadequate description of the performance of friction turbines. In fact, his experimental setup contains only two nozzles creating an inhomogeneous flow distribution. The theory instead assumes a homogeneous distribution of flow in circumferential direction. Only a test rig with the same boundary conditions will finally clarify these discrepancies. However, the Beans solution does not fully satisfy the incompressible Navier-Stokes-Equation, if inserted. The assumptions of parabolic velocity profiles in u- and v-direction, as well as the zero velocity assumption in z-direction represent the simplest assumption and do not agree well with CFD results. Improvements to this assumption are currently under investigation. This analysis still provides hints for maximum Tesla turbine performance in terms of the dimensionless parameters β, Ω and V_1. The economical power coefficient C_{pt} is finally a measure for rotor efficiency and will influence Tesla turbine geometry in the future. Nevertheless, it is possible to generate more absolute power per gap by applying a smaller radius r_2, but with a significantly higher pressure drop. A comprehensive and extended theoretical analysis including compressible effects and efficiency will be presented in a separate paper.

MECHANICAL DESIGN

Dimensioning the rotor. Based on the theory it was possible to design an application-oriented test rig to measure performance parameters as well as detailed velocity fields in the gap. The design criteria of the turbine have been defined as:

- adjustable and dismountable single-gap-rotor
- no disk-spacers at the inlet (no disturbance of flow)
- maximized optical accessibility
- low deformation of the single-gap-rotor under load
- adequate safety coefficient
- low vibration; low residual imbalance
- modular concept for future adaptions
- exchangeable guide vanes or nozzle
- turbine geometry according to dimensionless parameters
- adequate flow medium with $0 < \beta \leq 10$
- adjustable level of pressure and/or mass flow
- electric motor powering the rotor (instead of a generator)
- flexible design for a production-oriented multi-gap-rotor
- revolution speed for single-/multi-gap-rotor, no gearbox

With an existing, practically unlimited compressed air supply and the requirement of the medium fitting for PIV, air is chosen to be the operating medium. The technical design process of a Tesla turbine rotor is iterative. Fluid and turbine geometry are subjected to the definition of the dimensionless parameters β, Ω, V_1 and the manageable mechanical stress with a minimal deformation of the disks as a result of revolution speed. Fig. 7

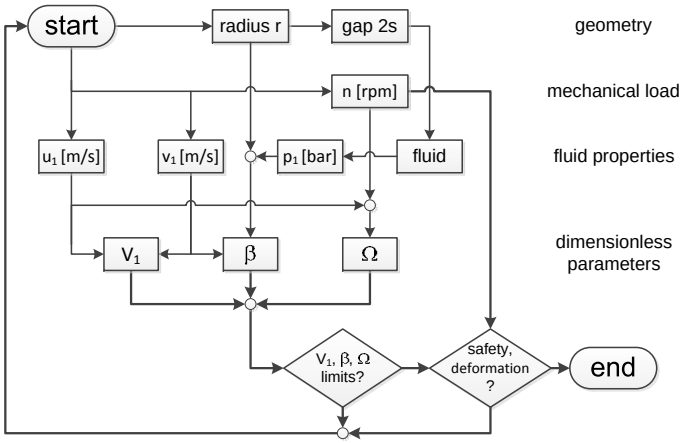

Figure 7. DIMENSIONING TURBINE GEOMETRY

illustrates the iterative turbine design process. For first estimations geometry (radius, gap width) and fluid properties (u_1, v_1, p_1) are chosen. Then the Beans solution predicts dimensionless parameters and turbine characteristics. After the definition of the mechanical load, the disk material and a technically feasible gap width, FEM tools compute mechanical stress, safety factor and deformation of the disks. The disk diameter was iteratively chosen with respect to the manageable mechanical stress and for optimal dimensionless parameters. Each iteration step includes a new mechanical rotor design in a CAD system. Maximum revolution speed limits the overall disk dimensions. Furthermore lu-

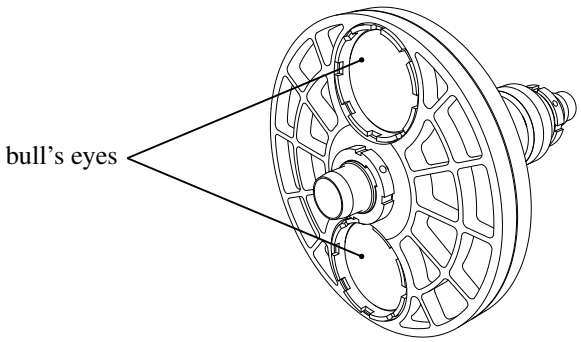

Figure 8. CAD-MODEL OF THE ROTOR

cent materials have to be used for optical velocity measurements in the gap. First designs applying acrylic glass failed due to too high mechanical stress as a consequence of high rev speed. The idea of a bull's eye as shown in Fig. 8 implied the use of steel as disk material. In order to achieve technically applicable and competitive turbines, β should be greater 10. But for $\beta \to \infty$, the gap width as well as mass flow and thus power go to zero. Fig. 9 shows achievable $\beta-$values with final rotor dimensions.

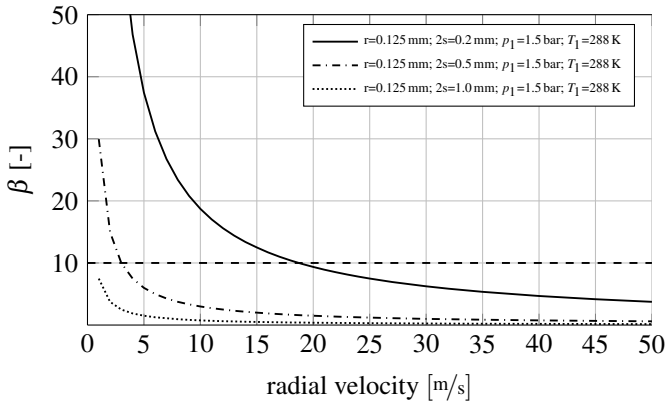

Figure 9. ACHIEVABLE VALUES OF β

Stress and deformation analysis. The mechanical design optimization of the rotor regarding mechanical stress and axial deformation has been accomplished using CAD and FEM tools. The best compromise between the lowest possible stress within the mechanical limits of steel, glass and the lowest axial deformation of the rotor disks has been found. Both disks cannot be designed identically (see Fig. 10). For the von-Mises stress computation, a minimum safety factor of 4.4 has been achieved. The rotor gap is closing (Δs) at the outer radius r_1 with increasing revolution speed. Tab. 1 shows the gap width blockage error e$(2s)$. The deformation in the middle sector between R=0.9

n	Δs	e$(0.2mm)$	e$(0.5mm)$	e$(1.0mm)$
4000 rpm	0.005 mm	2.5 %	1.0 %	0.5 %
6000 rpm	0.019 mm	9.6 %	3.8 %	1.9 %
8000 rpm	0.041 mm	20.5 %	8.2 %	4.1 %
10000 rpm	0.065 mm	32.5 %	13.0 %	6.5 %

Table 1. GAP WIDTH BLOCKAGE ERROR e$(2s)$

and R=0.3 is much lower compared to the rim region. Maximum power is expected to be at about 6000 rpm. The gap contraction is moderate at that speed (Fig. 10). Nevertheless, the relative gap width contraction error e$(2s)$ for gap widths of 0.2 mm and 0.5 mm above 10000 rpm is quite high. The simulations consider the mechanical loads due to rotation, preload forces due to shaft screw connection, gravity, the materials steel (disks, rings) and glass (windows) at ambient temperature. Both maximum values

of axial deformation and von-Mises-stress are converged with the refinement of the FE-grid. Fig. 10 exemplarily shows the axial deformation of the rotor disks at 6000 rpm.

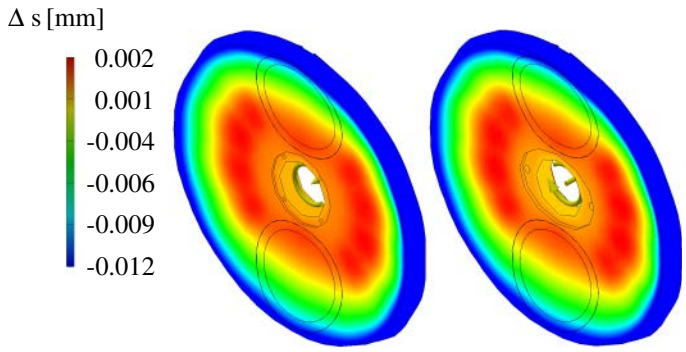

Figure 10. DEFORMED OUTER AND INNER DISK

Modal and harmonic response analysis. During the design process the eigenfrequencies always had to be considered. Therefore modal analyses have been carried out. The first mode was found far away from the operational range $(0-200\,\mathrm{Hz})$ at about 760 Hz. In a next step, the harmonic response analysis computes the amplitude response at a certain point at the outer disk-diameter (Fig. 11) as a result of harmonic excitation. On

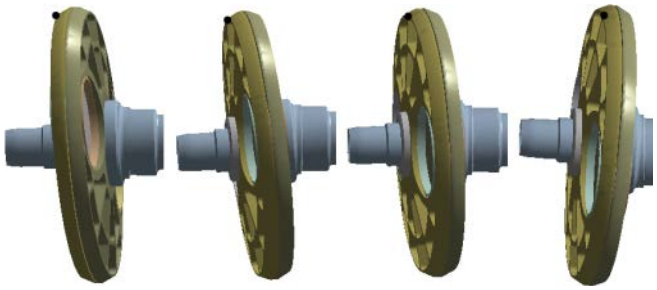

Figure 11. MODE OF MOTION AT 34 Hz

consideration of the manufacturing tolerances, the maximum imbalance of the rotor has been estimated. The space for material erosion has been defined in order to correct the maximum imbalance. The resulting residual unbalance has then been used as the oscillating load of the harmonic response analysis. Both analyses have been carried out with the ANSYS 14. However, the highest amplitude has been found at 34 Hz (see Fig. 11) with a phase angle change of 180°. A second harmonic analysis of the inner disk shows, that both disks are oscillating in phase with an amplitude of similar order. Since the magnitude of that frequency is extremely low and no eigenfrequency being found in that bandwidth of rev speed, the result was deemed acceptable. This frequency should be avoided during the measurements and driven through quickly. If vibrations occur, they will be detected by the measurement system for immediate emergency stop.

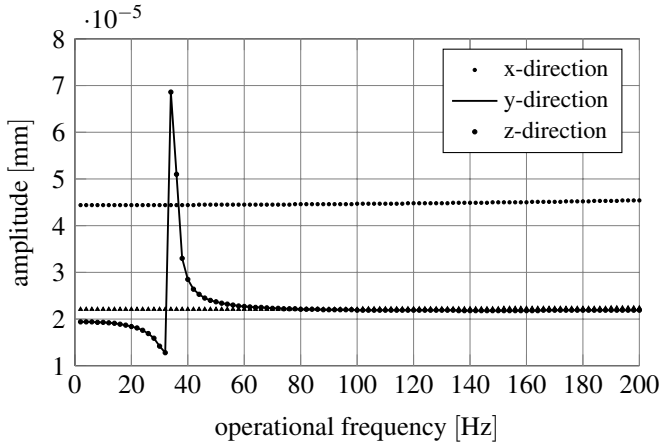

Figure 12. VIBRATION OF OUTER DISK

Design of the test rig. Fig. 13 shows the test rig with its main components in a lateral cut plane. The rotor is placed vertically in the center of the frame. Instead of braking the wheel, it is powered by a spindle motor, as there might not be enough energy extracted from the flow by only one gap to overcome bearing friction. On steady state flow conditions the expected flow field of the powered wheel is the same as if a generator was used. The frequency converter of the motor is equipped with resistors to operate as a generator for future multi-gap rotor applications. The flow enters an annular plenum through four inlets positioned

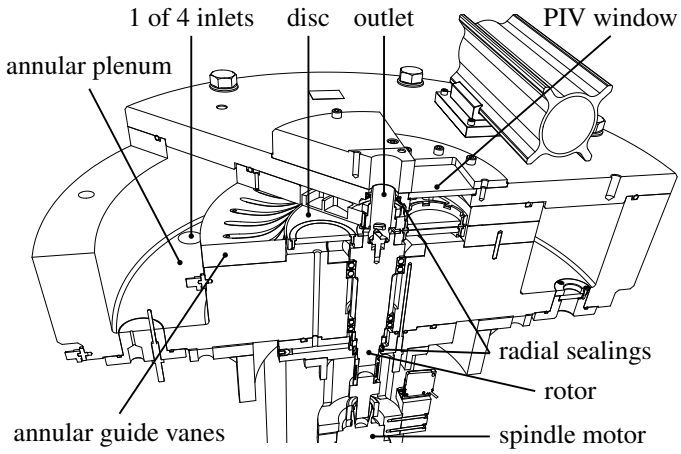

Figure 13. TEST FACILITY WITH MAIN COMPONENTS

evenly around the circumference. The plenum feeds the guide vanes, which impart the required swirl onto the flow. After passing the gap between the disks, the flow leaves the rotor through a hollow shaft in the center of rotation. The PIV cameras will be mounted just outside a glass window in the casing. The laser beam is coupled into the gap by a rotating mirror inside the hollow shaft. Guide vanes instead of nozzles are used to achieve a homogeneous rotor inflow. With a bigger inlet area the mass flow rate (Eq. 11) increases and therefore the torque and the power, too (Eq. 12, 13). Even if highest power is achieved at relatively high radius ratios R=0.85-0.90 (see Fig. 6), a lower outlet radius was chosen in order to understand the complete flow phenomena within a Tesla turbine. This is why a radius ratio of R=0.24 has been applied. The rig features exchangeable guide vanes and a dismountable rotor with variable gap width using different spacers at rev speeds from 0 to 12000 rpm. A flow regulator upstream the plenum sets the mass flow up to 0.17 $\frac{kg}{s}$.

The most critical point for a successful rig design is to manage leakage together with high rev speeds. Carbon floating seal rings resist huge rev speeds, but relatively high leakage ($< 5\,\%$) and the need for an enormous available space were unsatisfactory. Instead, high pressure PTFE radial shaft seal rings with very small shaft diameters for a minimal circumferential shaft speed offer leakages $\ll 1\,\%$ at pressure differences up to 10 bar with acceptable tear and costs. With a small pressure difference of < 2 bar the leakage mass flow is expected to be very low. This is sufficient enough for PIV measurements in the gap, but not for future turbine characteristic measurements. In that case, the leakage mass flows have to be measured. Also, a stack of disks instead of a single slot will be used for the investigation of the performance characteristics, which will increase the ratio of turbine mass flow to leakage mass flow. From a manufacturing point of view the smooth transition of the disk surfaces between steel and glass and to ensure that the gap of guide vanes and rotor fit together were the main problems.

MEASUREMENT AND CONTROL SOFTWARE

The test facility is controlled by a National Instruments Compact Reconfigurable In-/Output real-time system (cRIO) with an FPGA and in-/output devices. The measurement and feedback-control program sequence is shown in Fig. 14. A LabVIEW program running on a windows host machine provides the front end for the communication with the cRIO target, which records all sensor signals. The mass flow is controlled by a Bronkhorst flow regulator, its setpoint ($0-10\,\mathrm{V\,DC}$) can be adjusted in the host program. Selectively the regulator is able to handle the signal from the plenum pressure gauge as the controlled process variable. The revolution speed is controlled by a PID element on the FPGA. The cRIO provides the actuating variable for the frequency inverter which controls the motor. An optical rev meter makes the process variable available for the FPGA. The rotational speed of the rotor can be kept constant, if the air flow is switched on. A safety monitoring system including a security shutdown has been developed, in order to independently react on unsolicited vibrations. An envelope of failure of both bearings, which is used for the diagnosis of bearing failure is computed from two acceleration sensors positioned at 90° of each other in each case. The software also shuts down on high bearing temperatures or on hard- and software-panic-switch activity.

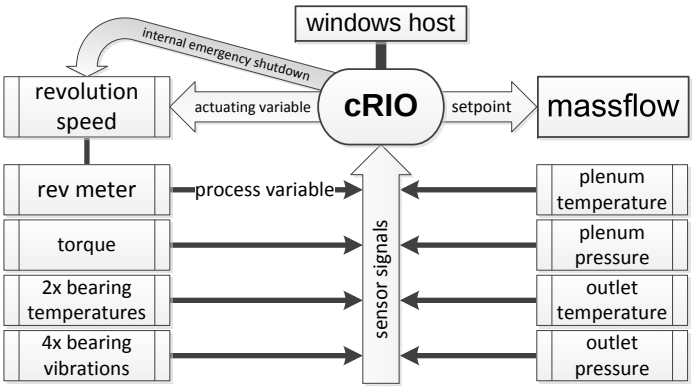

Figure 14. MEASUREMENT AND CONTROL SEQUENCE

PRELIMINARY PIV/PTV-MEASUREMENTS

To demonstrate the measurement technique, tests have been carried out in a simple geometry, see Schosser et. al. [10]. Fig. 15 exemplarily shows a captured laminar velocity profile normalized by the current maximum velocity (single shot). Two paral-

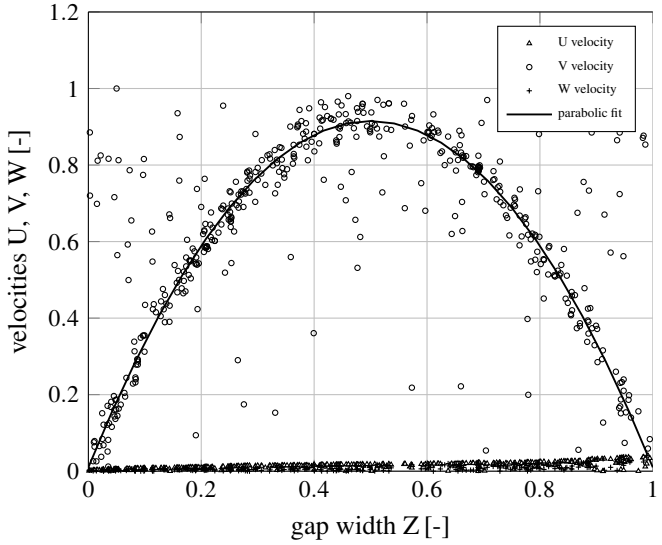

Figure 15. CAPTURED LAMINAR VELOCITY PROFILE

lel flat standard glass plates have been put together with spacers to build a channel with a cross-section of 75 mm x 1 mm and a length of 300 mm. The flow velocity is set by a simple pressure regulator, the compressed air enters the channel through an adapter. The goal of the setup was to demonstrate the measurement technique by capturing the laminar velocity profile in the gap of 1 mm. First attempts to apply a 3D stereo-PIV system failed because of the small seeding density. A cross-correlation could not be accomplished. With a limited optical access, the one camera astigmatistic 3D PIV method (Hain et. al. [11]) seemed to be the best approach. Unfortunately the reflections on the glass plates destroyed this hope as well. A four camera tomographic PIV system seemed impossible because of the restricted optical access in the turbine. It turned out, that the two camera setup provided the most promising attempt to measure the flow profile. The relatively low seeding density enabled a tomographic reconstruction. The peaks of the light intensity values of the reconstructed voxels were fit to particle positions and were tracked by an algorithm described by Cierpka et. al. [12].

CFD OPTIMIZATION OF RIG COMPONENTS

All computations have been carried out with ANSYS CFX 14. In all shown cases y+ has been adapted and the grid has been refined several times until the average outlet velocity has converged. Even if the power prediction is for laminar flow, turbulence models have always been applied. The critical Reynolds number for the plane channel flow found by Carlson et. al. [13] is ≈ 670. Takeishi et. al. [14] examined the influence of rectangular-ducts with different aspect ratios using DNS. A good agreement with Carlson et. al. has been found for aspect ratios > 5. The Reynolds number is defined with the mean velocity and half of the duct height resp. half of the gap width. As the CFD Reynolds numbers of the turbine are always above the critical one, turbulent flow is expected at all revolution speeds (see Tab. 2). Nevertheless, it is not sure if the classical transitional mechanisms are applicable, due to acceleration of the flow and fictitious forces. This has to be clarified during the flow field measurements of the rotor. Here, CFD has been used for optimizing rig components.

n	1000	2000	3000	5000	7000	9000	10000
Re	2097	2130	2159	2219	2283	2385	2446

Table 2. REYNOLDS NUMBERS IN TURBINE, CFD RESULTS

Flow through plenum. The flow inside the plenum (see Fig. 13) and through the guide vanes has been examined to demonstrate a homogeneous mass flow distribution at the outlet of the guide vanes. The CFD settings are:

- ideal gas, total energy, SST turbulence model
- auto timescale
- domain 90° section (1:1 periodic)
- domain with 3.2 million cells
- inlet: $\dot{m} = 0.02\,\mathrm{kg/s}$, outlet: $p_2 = 1.2\,\mathrm{bar}$
- residual convergence: $1 \cdot 10^{-5}$ rms and $1 \cdot 10^{-3}$ max

A typical value has been chosen for the static outlet pressure p_2 from earlier computations at that point. Four 90°-shifted inlets supply the plenum with compressed air. The total area of the inlets into the plenum is slightly bigger than the area of the inlet to the guide vanes in order to generate a small pressure drop, which helps the flow to be homogeneously and circumferentially distributed. The flow subsequently enters the guide vanes. The streamline plot through plenum and guide vanes indicates a good mixing upstream the guide vanes (Fig. 16). Although the wakes

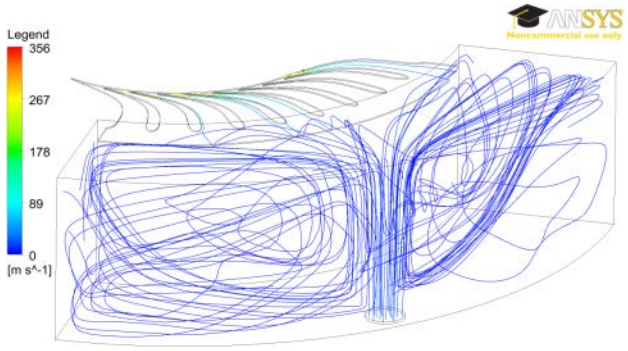

Figure 16. STREAMLINES IN PLENUM, GUIDE VANES

of all inlet guide vanes are clearly visible (Fig. 17), the mass flow distribution is circumferentially periodic, homogeneous and sufficient for PIV applications in the gap.

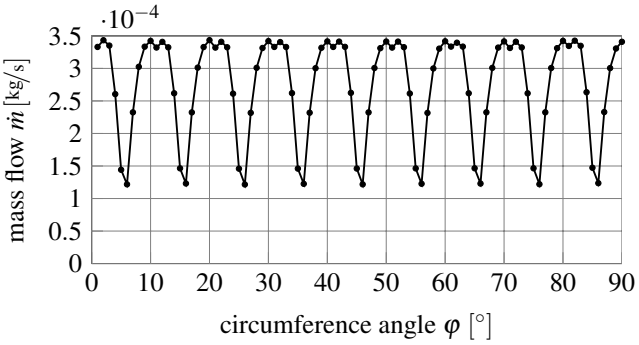

Figure 17. MASS FLOW DISTRIBUTION, STATOR OUTLET

The mass flow shown here is averaged over the area *gap width* $\times$ *arc length of 1°*.

Optimization of guide vanes. In a next step the guide vanes (Fig. 13) have been optimized to yield the disk inlet flow angle according to the theoretical calculations. With $V_1 = 0.3$, the flow exit angle of the guide vanes is $\alpha_f = 16.7°$. The profile is designed with the use of splines. The flow inlet direction is completely radial, the leading edge form is chosen to be elliptic. The geometric exit angle α_g has been set to the same value as the ideal flow output angle α_f. The number of blades is 36, rotor and stator gap width 2s is 0.5 mm. First computations were used to adapt the chord length, as well as the curvature of pressure and suction side in order to generate uniform flow without separations, which would block the guide vanes. As the average flow exit angle α_f differed from the geometrical exit angle α_g, the geometrical exit angle α_g has iteratively been adapted. The rotational frequencies of the rotor domain have been varied. The CFD settings are:

- ideal gas, total energy, k$-\omega$ turbulence model
- local timescale (CFL=1 up to 20)
- frozen rotor (ggi) interface with pitch ratio 1.0
- rotor, stator domain each 90° sections (1:1 periodic)
- rotor and stator domain with 3 million cells
- rotor domain motion 1000 to 10000 rpm
- initial values from last computation (except 1000 rpm)
- inlet: $\dot{m} = 0.02\,\mathrm{kg/s}$, outlet: $p_2 = 1.0\,\mathrm{bar}$
- residual convergence: $1 \cdot 10^{-5}$ rms and $1 \cdot 10^{-3}$ max

The flow angle α_f or V_1 changes with the angular velocity. The theoretical optimum is hit at high rev speeds between 7000 and 10000 rpm. The direction of inflow and therefore the guide vane design is satisfactory, because maximum power is found in that range (see Fig. 23). The dimensionless parameters calculated from CFD results are presented in Tab. 3. The flow through

n	1000	2000	3000	5000	7000	9000	10000
V_1	0.34	0.34	0.33	0.32	0.31	0.29	0.29
β	1.1	1.1	1.1	1.1	1.1	1.1	1.1
Ω	0.16	0.31	0.47	0.80	1.15	1.50	1.69

Table 3. DIMENSIONLESS PARAMETERS, CFD RESULTS

the CFD-optimized guide vanes and the rotor with different rotational speeds is visualized in Fig. 18. The reference frame of the rotor streamlines shown here is absolute.

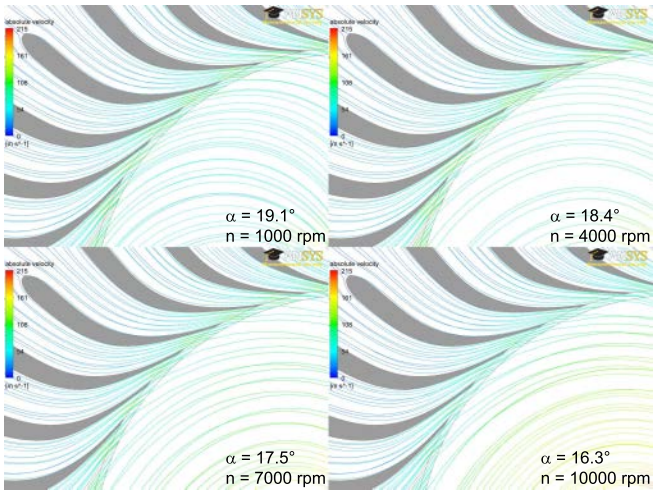

Figure 18. STREAMLINE PLOT OF STATOR AND ROTOR

Optimization of disk rotor outlet. The design of the disk rotor outlet at the inner edge of the gap between the disks has been adapted for a correct exit swirl angle to minimize the flow losses. The inner disk is bolted to the outer disk via an oval, exchangeable spacer (Fig. 19). In order to provide different gap widths

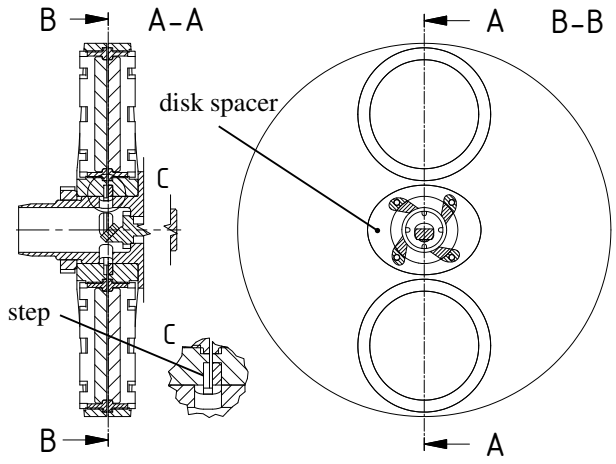

Figure 19. ROTOR WITH DISK SPACING OUTLET

and an accurate rotor-restraint at the same time, an abrupt step of 2 mm in z-direction becomes necessary. Although the flow is disturbed, the transmission of the frictional force is limited at a defined radial position - independent from the desired gap width. The shape-optimized spacers (see Fig. 19) channel the flow into the hollow shaft without compromising its mechanical functions. The angle of attack fits all rev speeds, especially at maximum power (see Fig. 20). The separations near the outlet are origi-

nated by the axial step. At least here, the flow is turbulent.

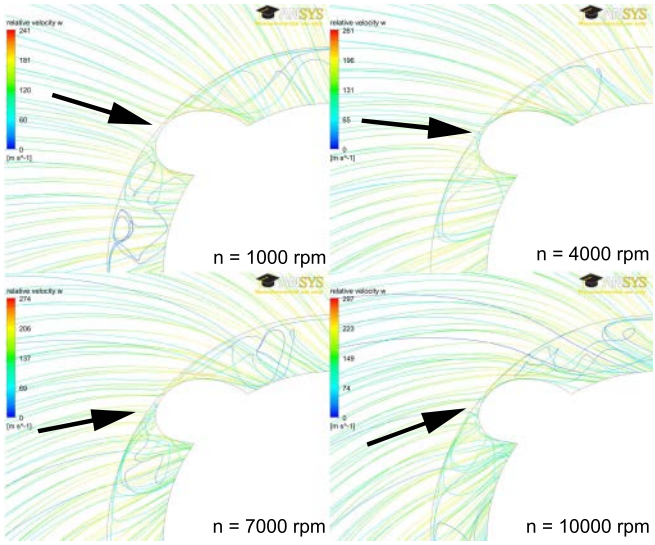

Figure 20. RELATIVE STREAMLINES IN ROTOR OUTLET

Rotor inflow behavior. Fig. 21, 22 show the development of velocity profiles inside the rotor at different radial positions and low and high revolution speeds. The relative velocity is made

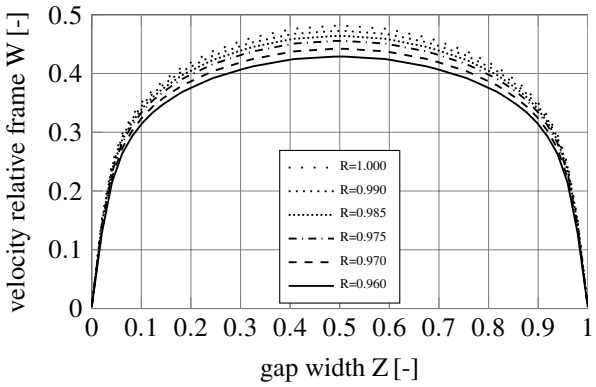

Figure 21. RELATIVE VELOCITY PROFILES, 1000 RPM

dimensionless with the maximum velocity at its rotor outlet. The fully developed velocity profile is obtained at the radius ratio of R = 0.96 at high and low rev speeds. The radial length of its run-in distance is low compared to the entire rotor radius. The optical access in the rotor for capturing the velocity profiles with 3C-PIV is between R = 0.91 and R = 0.33 .

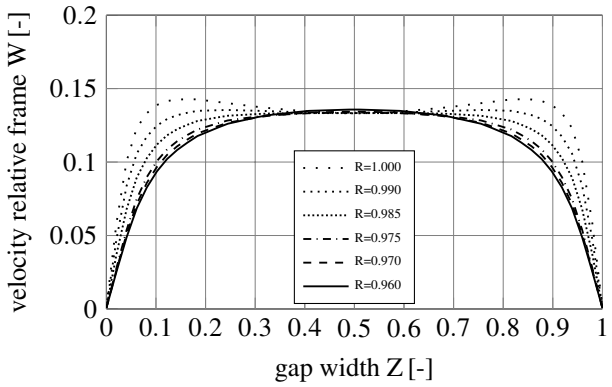

Figure 22. RELATIVE VELOCITY PROFILES, 8000 RPM

Turbine characteristics. The characteristic maps of the Tesla turbine computed from Eq. 7 (see [7]) and derived from the CFD is presented in Fig. 23. Both solutions provide the same inflow conditions as used in CFD optimization before. In both cases

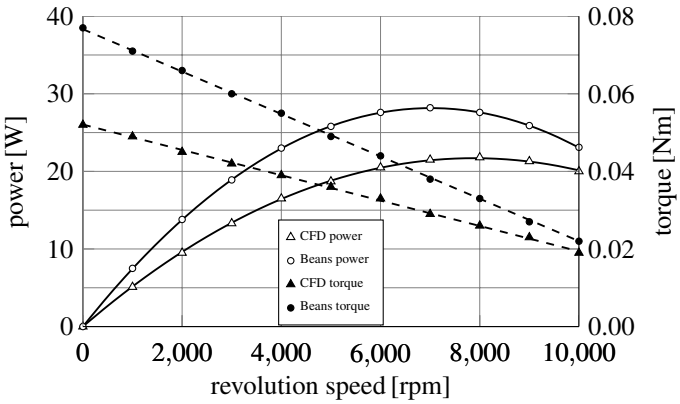

Figure 23. CHARACTERISTIC MAP OF TURBINE

maximum torque is found at zero rotation, linearly decreasing with rotational speed. Power is quadratically increasing with rotational speed, as Beans [7] predicted. The relative rotor velocity streamlines at different operational speeds are shown in Fig. 24. At a lower rotational speeds, the relative velocity is high and for this reason the torque. In terms of CFD, Fig. 23 and 24 indicate that the lowest relative velocity occurs near maximum power ($8000\,\text{rpm}, \Omega \approx 1.3$). With values of $\Omega > 1$, the relative circumferential velocity has to change its algebraic sign, according to the velocity triangles. Even if the flow decelerates the disks at the outer rim region, the total torque integrated over the whole radius is still positive. The CFD power peak is at slightly higher rev speeds, as predicted. One explanation is, that the analytical solution is computed incompressible without considering the

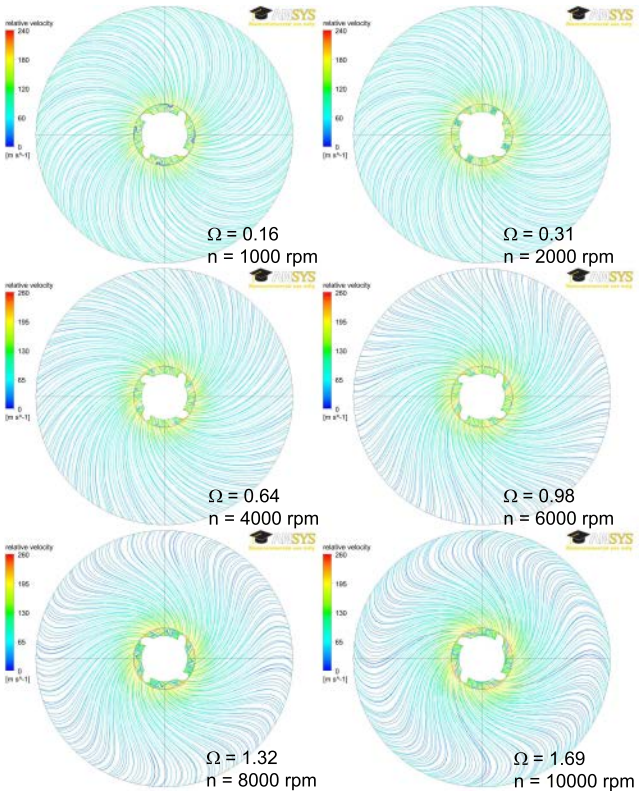

Figure 24. RELATIVE STREAMLINE PLOT IN ROTOR (CFD)

energy equation. Another difference is the laminar flow assumption without any development of the velocity profile. The Beans solution neglects wakes of the guide vanes at the rotor inlet and influences of the flow in the gap caused by the rotor outlet design. In spite of slightly overpredicting Tesla turbine characteristics, the analytical solution turns out to be suitable as a power output estimation with a very short computation time for various applications. Nevertheless, the present simulation is a low-β examination. A high-β computation for the adaption of the second guide vanes is currently in progress.

CONCLUSION AND PROSPECTS

The theoretical investigations of the Tesla turbine, which proved to be a good power output prognosis, enabled the actual design process of the test rig. Between functionality, mechanical limitations and cost pressure, a good compromise was found. CFD helped to optimize the flow through stator and rotor. The measurement method has successfully been demonstrated and the control software works properly. It will be the first time to measure the real flow field inside the gap of a technically reasonable design of a Tesla turbine. The results from the PIV measurements in the rotor will certainly be exciting, since it will allow the validation of the CFD. Until the turbine is manufactured, a multi-gap rotor with an optimum radius ratio is designed for future characteristic map investigations. During that time the CFD investigations will be continued and improved. The buildup starts in December 2013, the PIV tests are planned for March 2014.

ACKNOWLEDGMENT

Thanks go to Prof. Dr. rer. nat. C. Kähler and Dr.-Ing. R. Hain for supporting the PIV tests and to Dipl.-Ing. K. Dingeldein for his advice in terms of mechanical design.

REFERENCES

[1] Tesla, N., 1913. Tesla turbine, May 6. US Patent 1,061,142.

[2] Romanin, V. D., and Carey, V. P., 2011. "An integral perturbation model of flow and momentum transport in rotating microchannels with smooth or microstructured wall surfaces". *Physics of Fluids,* ***23***, p. 082003.

[3] Lampart, P., and Jedrzejewski, L., 2011. "Investigations of aerodynamics of tesla bladeless microturbines". *Journal of Theoretical and Applied Mechanics,* ***49***, pp. 477–499.

[4] Khan, M., Maqsood, M., Ali, E., Jamal, S., and Javed, M., 2013. "Proposed applications with implementation techniques of the upcoming renewable energy resource, the tesla turbine". *J. Phys.: Conf. Ser.,* ***439***, p. 012040.

[5] Breiter, M. C., and Pohlhausen, K., 1962. Laminar flow between two parallel rotating disks. Tech. rep., DTIC doc.

[6] Rice, W., 1965. "An analytical and experimental investigation of multiple-disk turbines". *J. Eng. Power,* ***87***, p. 29.

[7] Beans, W., 1966. "Investigation into the performance characteristics of a friction turbine.". *JSpRo,* ***3***, pp. 131–134.

[8] Nendl, D., 1973. "The tesla turbine". *VDI Tagung,* ***193***, pp. 287–293.

[9] Nendl, D., 1976. "Three-dimensional laminar instabilities at flat walls". In GAMM W. Paris France, Vol. 56, p. 211.

[10] Schosser, C., and Hain, R., 2013. "Determination of velocity profiles in small gaps between parallel flat plates by means of tomografic piv". *Fachtagung Lasermethoden der Strömungsmesstechnik,* ***21***.

[11] Hain, R., Kähler, C. J., and Radespiel, R., 2009. "Principles of a volumetric velocity measurement technique based on optical aberrations". In *Imaging Measurement Methods for Flow Analysis*. Springer, pp. 1–10.

[12] Cierpka, C., and Kähler, C. J., 2012. "Particle imaging techniques for volumetric three-component (3d3c) velocity measurements in microfluidics". *JOV,* ***15***(1), pp. 1–31.

[13] Carlson, D. R., Widnall, S. E., and Martin, F. P., 1982. "A flow-visualization study of transition in plane poiseuille flow". *JFM,* ***121***, pp. 487–505.

[14] Takeishi, K., Kawahara, G., Uhlmann, M., Pinelli, A., and Goto, S., 2012. "Puff-spot transition in rectangular-duct flows". In JSST, p. 197.